Bright, photostable, and long-circulating NIR-II nanoparticles for whole-process monitoring and evaluation of renal transplantation

Authors: Rongyuan Zhang[1,2]†, Ping Shen[3]†, Yu Xiong[2]†, Tianjing Wu[3], Gang Wang[3], Yucheng Wang[1], Liping Zhang[1,2], Han Yang[1], Wei He[4,5], Jian Du[6], Xuedong Wei[6], Siwei Zhang[5], Zijie Qiu[1], Weijie Zhang[6]*, Zheng Zhao[1,4]*, Ben Zhong Tang[1,5]*

Affiliations:

[1]School of Science and Engineering, Shenzhen Institute of Aggregate Science and Technology, The Chinese University of Hong Kong, Shenzhen, Guangdong 518172, China.

[2]Center for AIE Research, Shenzhen Key Laboratory of Polymer Science and Technology, Guangdong Research Center for Interfacial Engineering of Functional Materials, College of Materials Science and Engineering, Shenzhen University, Shenzhen 518061, China.

[3]School of Chemistry, Xiangtan University, Xiangtan, 411105, China.

[4]HKUST Shenzhen Research Institute, Shenzhen 518057, China.

[5]Department of Chemistry, Hong Kong Branch of Chinese National Engineering Research Center for Tissue Restoration and Reconstruction, The Hong Kong University of Science and Technology, 100071 Hong Kong, China.

[6]Department of Urology the First Affiliated Hospital of Soochow University Suzhou 215006, China.

†These authors contributed equally to this work.

*Corresponding author. Email: tangbenz@cuhk.edu.cn (B.Z.T.); zhaozheng@cuhk.edu.cn (Z.Z.); wj539@163.com (W.J.Z.).

One Sentence Summary: The current work pioneers the monitoring and evaluation the whole process of renal transplantation in vivo using the NIR-II fluorescence technology.

Abstract: Kidney transplantation is the gold standard for the treatment of end-stage renal disease (ESRD). However, the scarcity of kidneys has caused more and more ESRD patients being stuck

on the waiting-list for surgery. Improving the survival rate of kidney grafts as much as possible is not only responsible for patients, but also an alternative solution to kidney shortage. Thus, rapid diagnosis and timely management of surgical complications are of vital importance to the success of renal transplantation but lack efficient methods and technologies. Herein, a fluorescence technology based on bright, photostable, and long-circulating aggregation-induced emission (AIE) active NIR-II nano contrast agent for the whole-process monitoring and evaluation of renal transplantation has been reported. The outstanding optical property and long-circulating characteristic of the AIE NPs help to achieve renal angiography in the kidney retrieval surgery, donor kidney quality evaluation before transplantation, diagnosing vascular complications, and assessment of renal graft reperfusion after revascularization, which considerably outperforms the clinically approved indocyanine green (ICG).

INTRODUCTION

Medicine and surgery are the primary treatments of modern diseases. However, for some end-stage organ diseases like end-stage renal disease (ESRD), organ transplantation has been acknowledged as the most effective and the life-saving treatment (*1, 2*). According to the Chinese Scientific Registry of Kidney Transplantation (CSRKT) data, approximately 11,000 patients with ESRD received a kidney transplant in 2020, while more than 60,000 patients remain on a waiting list for renal transplantation (*3*). The dilemma of kidney source scarcity is also suffered by people of the other countries of the world (*4, 5*). In consideration of the organ shortage issue worldwide, improving the success rate of organ transplant become highly significant (*6*).

The operation of kidney transplants involves donor kidney retrieval (donor nephrectomy), donor kidney preservation, and vascular and ureteric reconstruction (*7*). Among them, the quality of a donor's kidney directly influences the outcome of the transplantation. Furthermore, the anastomosis of vascular and ureterovesical also affects the reperfusion and urine excretion of implanted kidneys, which play a significant role for a successful renal transplantation surgery (*8, 9*). Therefore, real-time evaluation and monitoring the reperfusion and urine excretion of kidney before, during and after the kidney implant will benefit a lot for increasing the success rate of renal transplant surgery. Traditionally, the patency of the vascular anastomosis was determined by visual inspection of arterial pulse quality, venous filling, color, and turgidity of the renal graft (*10*), which mainly depended on the surgeons' experience and easily led to incorrect identification. Although imaging techniques like Doppler ultrasound, X-ray angiography (*11*), computed tomography (CT)

(*12*), magnetic resonance imaging (MRI) (*13*), and radionuclide imaging (*14*) could be used for diagnosing surgical complications and assessing renal graft reperfusion, most of them have limitations for real time monitoring and tracing and may even suffer the drawbacks of radioactive injure (*15*), expensive costs, and cumbersome operations. In terms of these, fluorescence imaging technology has emerged as an ideal pathway for in situ and real time monitoring various diagnosis or therapeutic processes such as cancer imaging in oncological surgeries, angiography and intraoperative identification of ureters (*16, 17, 18*). Therefore, utilizing fluorescence imaging technology to evaluate the reperfusion of donor kidney and monitor the anastomosis of vascular and ureterovesical provides a feasible approach to improve the success rate of renal transplantation surgery.

Fluorescence imaging technology strongly relies on imaging contrast agents. In particular, organic luminogens with second near-infrared region (NIR-II, 1000-1700 nm) absorption and emission are highly desirable contrast agents due to their excellent biocompatibility, deep penetration depth and high imaging contrast (*19, 20, 21*). Although organic NIR-II luminogens have demonstrated their significant applications as fluorescent contrast agents, the commonly used commercial imaging contrast agents like ICG suffer the problem of concentration quenching effect, which means they can only be used in low concentration since high concentration will diminish and even quench the emission (*22*). Low concentration administration and rapid hepatobiliary clearance (*23, 24*) result in a significantly reduced imaging window of ICG (less than 5 minutes) (*25*), which is inadequate to guide a 3.5 - 5 hours (*26*) of kidney transplant surgery. Although the photostability of the molecular contrast agents could be improved by preparing their nanoaggregates, the aggregation mostly reduced the brightness of traditional planar luminogens including ICG, which limit their application for long-time surgical process imaging and monitoring. In this regard, NIR-II luminogens with high brightness, long-circulating time, and high photostability in aggregates are highly desirable.

Aggregation-induced emission (AIE) luminogens are a kind of unique luminescent materials with aggregation-enhanced photoluminescence quantum efficiency and photostability, which may work as ideal candidates to prepare NIR-II emissive nano contrast agents with high brightness and superior photostability (*27*). It is worthy to note that the brightness of a luminogen mainly depends on the production of the molecular absorptivity and photoluminescence quantum yield (PLQY) (*28*). However, current molecular design of AIEgens mostly requires the introduction of highly

twisted molecular rotors to avoid the strong intermolecular interaction-caused luminescence quenching effect, which unfortunately usually results in a relatively lower molar absorptivity (*29*). Therefore, how to design AIE luminogens with both high molar absorptivity and high PLQY is still a big challenge.

Fused-ring electron acceptors (FREA) for organic solar cell applications have rapidly developed in recent years whose absorption wavelength mainly locate in NIR region with superior light-harvesting capability (*30*). However, the luminescence properties of these materials have scarcely been investigated and applied in biomedical area. In this work, by learning from the molecular design of FREA, we designed and synthesized two-expanded molecules DIPT-IC and DIPT-ICF with rigid and planar conjugation structures. The results indicate that both DIPT-IC and DIPT-ICF exhibit NIR-II emission and AIE property with superior absorptivity and high PLQYs, which endow them with high brightness and superior photostability in aggregates. Water soluble nanoparticles of DIPT-IC and DIPT-ICF thus were prepared and applied in monitoring and evaluation of the entire process of kidney transplantation. The results indicate that a single dose of DIPT-ICF NPs contrast agent could monitor the entire surgical process very clearly via luminescence, which is much better than the commercial contrast agent ICG. This study demonstrates that fluorescent imaging technology based on NIR-II contrast agents is a promising approach to monitor the whole process of organ transplantation surgery and diagnose the possible surgical complications, which would work as a reliable approach to assist surgeons to improve the success rate of renal transplantation.

RESULTS
Synthesis and characterization
Two-expanded acceptor-donor-acceptor molecules DIPT-IC and DIPT-ICF have been designed and synthesized. The synthetic routes were shown in scheme S1. Compound **1** was synthesized according to literature method (*31*). Suzuki coupling between compound **1** and methyl 2-bromothiophene-3-carboxylate gives intermediate **2**. The intermediate **2** further reacts with 1-bromo-4-hexylbenzene in the presence of n-BuLi, affording fused-ring intermediate **3**. Compound **3** undergoes Vilsmeier-Haack reaction and produces DIPT-CHO. Finally, Knoevenagel reaction between DIPT-CHO and Indanone-cyano derivatives afford the two targeting molecules DIPT-IC and DIPT-ICF. All the intermediates and target molecules have been characterized by ^{1}H NMR, ^{13}C NMR and Mass spectra (Fig S19-S33).

The optical properties of DIPT-IC, DIPT-ICF, and their nanoparticles (NPs) were investigated by UV-vis and photoluminescence (PL) spectroscopy (Fig. 1). The NPs of DIPT-IC and DIPT-ICF were fabricated by nanoprecipitation method using the FDA-approved surfactant F-127, and the sizes of which were analyzed by dynamic light scattering (DLS) and transmission electron microscopy (TEM) (Fig. 1A, 1B and S1). Both DIPT-IC and DIPT-ICF showed strong absorption in tetrahydrofuran solution with maximal absorption peaks of 746 nm and 818 nm, respectively. Compared with the non-fluorinated molecule DIPT-IC, the absorption of the fluorinated molecule DIPT-ICF showed a redshift of 72 nm, which could be ascribed to the enhanced the intramolecular charge transfer (ICT) effect induced by the electron-withdrawing fluorine atoms (*32*). Density functional theory (DFT) calculation reveals that DIPT-ICF exhibits smaller energy gap than DIPT-IC (1.844 eV vs 1.879 eV) (Fig. S2), which matched well with the absorption data. Moreover, the
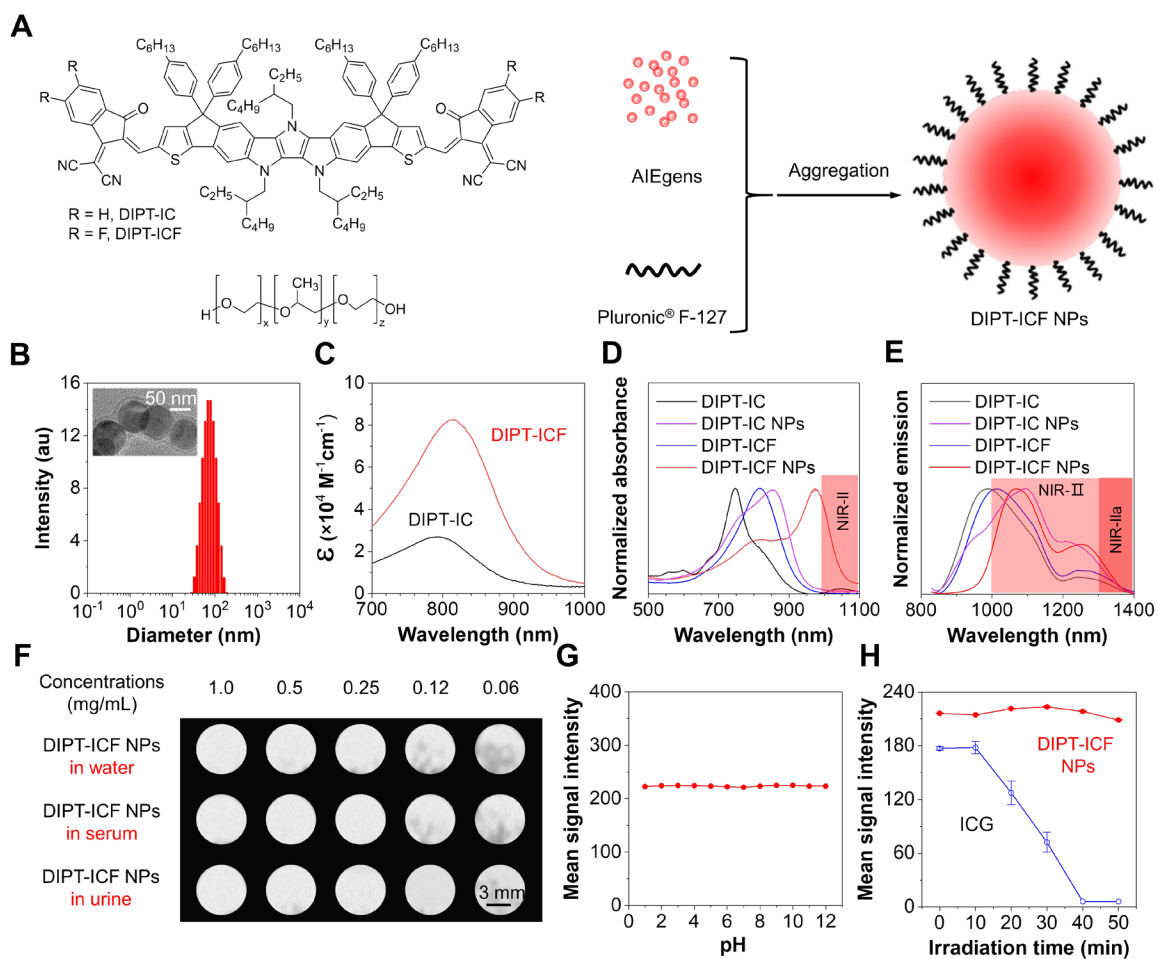

Fig. 1. Preparation and characterization of DIPT-ICF NPs. (**A**) Schematic illustration for the synthesis of DIPT-IC and preparation of DIPT-ICF NPs. (**B**) Dynamic light scattering (DLS) data and transmission electron

microscopy (TEM) image (the scale bar of the inset indicates 50 nm) of DIPT-ICF NPs. (**C**) Molar absorptivity of DIPT-IC and DIPT-ICF. (**D**) Absorption spectra of DIPT-IC and DIPT-ICF solutions (in THF) and their NPs in deionized water. (**E**) Emission spectrum of DIPT-IC and DIPT-ICF in THF and their NPs in deionized water. (**F**) NIR-II images of DIPT-ICF NPs in deionized water, serum, and urine with different concentrations (1, 0.5, 0.25, 0.125 and 0.0625 mg/mL), using a 980 nm laser as excitation source with a power density of 60 mW/cm^2 (the scale bar indicates 3 mm). (**G**) Mean signal intensity of DIPT-ICF NPs in NIR-II window at different pH states. (**H**) Photostability measurement of DIPT-ICF NPs and ICG upon irradiation with 808 nm laser with a time interval of 10 min at a power density of 100 mW/cm^2.

well overlapped highest occupied molecular orbital (HOMO) and lowest unoccupied molecular orbital (LUMO) electron density distribution suggests a favorable electron transition, which benefits a high molar absorptivity. Indeed, the molar absorptivity of DIPT-ICF is as high as 8.23×10^4 M^{-1}cm^{-1}, which is higher than that of DIPT-IC 2.43×10^4 M^{-1}cm^{-1}, suggesting that the introduction of fluorine atom helps to improve the molar absorptivity (Fig. 1C). Therefore, the introduction of fluorine atom benefits both the absorption redshift the molar absorptivity enhancement. It is worthy to note that molar absorptivity of over 80000 M^{-1}cm^{-1} is rather high for NIR-II luminogens, which will contribute greatly to the brightness of the contrast agents (*33*). After encapsulating with F127, both the absorption of DIPT-IC NPs and DIPT-ICF NPs exhibit obvious redshifts relative to their molecular species, in particular, the absorption peak of DIPT-ICF NPs can even shift to 974 nm with the tail extending to 1100 nm, which is favorable for achieving deep penetration depth for in vivo imaging (Fig. 1D).

The PL property of solution and NPs of DIPT-IC and DIPT-ICF were investigated. As shown in Fig. 1E, the main emission maxima of DIPT-IC and DIPT-ICF have been recorded as 988 nm and 1014 nm, respectively, while the emission of their NPs redshifted to 1090 nm and 1078 nm, respectively, due to the enhanced intermolecular interactions in aggregate state. It is worthy to note that both DIPT-IC and DIPT-ICF as well as their NPs exhibited shoulder peaks extended to the NIR-IIa region (1300-1400 nm), which were much favorable to achieve a deep penetration depth for in vivo imaging. PLQY (Φ_{PL}) of DIPT-IC and DIPT-ICF were determined to be 1.86% and 0.66%, respectively, both of which are higher than the reference molecule IR-26 ($\Phi_{PL} = 0.5\%$) (*34, 35*) (Fig. S3). Although the PLQY of DIPT-ICF is slightly lower than that of DIPT-IC, its brightness is much higher than that of DIPT-IC since brightness is the production of molar absorptivity and PLQY (*36*), while the molar absorptivity of DIPT-ICF is 3.4 times higher than

that of DIPT-IC. The aggregation-enhanced emission properties (Fig. S4) and high brightness of DIPT-ICF demonstrates its potential as high brightness fluorescence nano contrast agent.

Fluorescence intensity measurement of DIPT-ICF NPs in the NIR-II Window

The high brightness of DIPT-ICF NPs (Fig. S5) further inspire us to explore its imaging performance as fluorescent contrast agent. Fig. 1F and Fig. S6A show that the fluorescence signal DIPT-ICF NPs was gradually enhanced with increasing the molecular concentration and afforded stable fluorescent signals in different aqueous media, suggesting the superior stability of these fluorescent nano contrast agent in the body fluid environment. Since the pH value of interstitial fluid varies with organ metabolism, the PL intensity of DIPT-ICF NPs under different pH was also investigated, which was almost unchanged when varying the pH from 1 to 12 in phosphate buffered solution (PBS), demonstrating the excellent stability of DIPT-ICF NPs upon pH variation (Fig. 1G; S6, C and D). Photostability of the imaging contrast agent is also significant for biological process monitoring or guiding the surgery since poor photostability suffers the photobleaching effect when implementing the long-time imaging. Upon continuous laser irradiation, DIPT-ICF NPs revealed superior photostability compared with ICG in an aqueous environment, which is beneficial for application scenario of continuous imaging events, long-circulating fluorescence angiography and so on (Fig. 1H; S6E). Noteworthy, DIPT-ICF NPs don't not exhibit a significant photothermal effect at low energy density ($\sim$100 mW/cm^2), which would not cause thermal damage to living tissues during the imaging process (Fig. S7).

Tissue phantom imaging in vitro and vascular angiography in vivo in NIR-I/II windows

The high brightness, long absorption and emission wavelength, as well as the superior stability of DIPT-ICF NPs makes it excellent imaging contrast agent for implementing the whole organ transplantation surgery. Before applying DIPT-ICF NPs for in vivo experiment, the penetration depth and imaging resolution of DIPT-ICF NPs were evaluated in vitro through tissue phantoms (*37*). As shown in Fig. S8A, pre-covering DIPT-ICF NPs filled capillary tubes with chicken breast tissue, the signal background ratios (SBRs) of NIR-I and NIR-II imaging were measured. The fluorescence signals intensity collected from both NIR-I and NIR-II channel were obvious when the chicken breast tissue thickness is smaller than 2 mm (Fig. S8, B and C). When the thickness of chicken breast tissue was increased to 3 mm, NIR-II imaging exhibited its advantage in penetration depth with SBRs of NIR-II significantly higher than that of NIR-I (P < 0.05) (Fig. S8D). To further

evaluate the potential of DIPT-ICF NPs for angiography in vivo, subcutaneous fluorescent angiography was performed on mice abdomens under different laser-filter arrays, such as 808 nm laser combined with 900 nm long pass filter (LP) and 1319 nm LP, and 980 nm laser combined with 1020 nm LP, 1100 nm LP, and 1319 nm LP, respectively (Fig. 2, A and B). In general, the combination of 980 nm laser excitation and 1319 nm LP affords higher resolution angiography images and better SBR, which can be assigned to the higher brightness and deeper penetration depth in this wavelength region (Fig. 2, C and D).
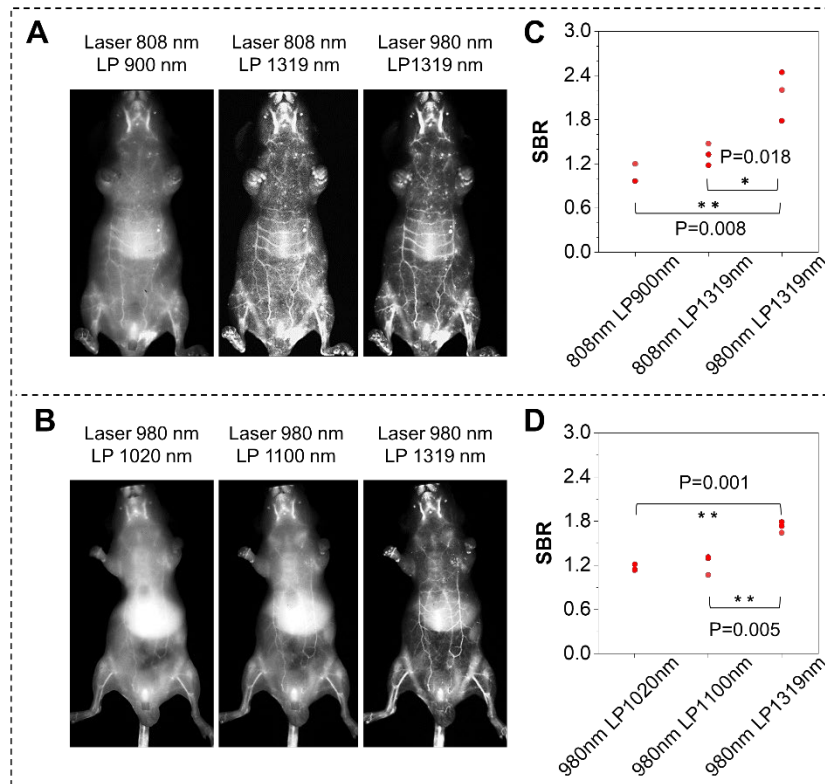

Fig. 2. NIR-I/II subcutaneous angiography with DIPT-ICF NPs in mice. (**A**) NIR-II subcutaneous angiography was performed on mice abdomens under various lasers and filters arrays, such as 808 nm laser with 900 nm long pass filter (LP 900 nm), 808 nm laser with 1319 nm long pass filter (LP 1319 nm), and 980 nm laser with LP 1319 nm. (**B**) NIR-II subcutaneous angiography was performed on the abdomen of mice under a 980 nm laser with LP 1020 nm, LP 1100 nm, and LP 1319 nm. (**C, D**) Quantitative analysis indicated that the SBR of angiography under the parameter of 980 nm laser with LP 1319 nm was highest among all the arrays. Significance was calculated by a Student's t-test. **$P < 0.01$, *$P < 0.05$.

Blood circulation time test and long-circulating angiography of subcutaneous vasclatures in mice and rabbits

To achieve the whole process monitoring and evaluation of renal transplantation surgery through fluorescence, long circulation time of contrast agents in the bloodstream is necessary. Intravenous injection of 60 µg (0.3 mg/mL in PBS, 200 µL per mouse) DIPT-ICF NPs into Balb/c nude mice, strong fluorescent signal of DIPT-ICF NPs could be observed from the serum even after 24 hours' circulation in blood (Fig. 3A). As a contrast, when 200 µl of ICG aqueous solution were injected into Balb/c nude mice, a relatively weak fluorescent signal could be observed from serum which started to decay after 30 min (Fig. 3B). Comparison between the mean fluorescence signal intensity of ICG and DIPT-ICF NPs contained in the serum indicated that both the fluorescent intensity and
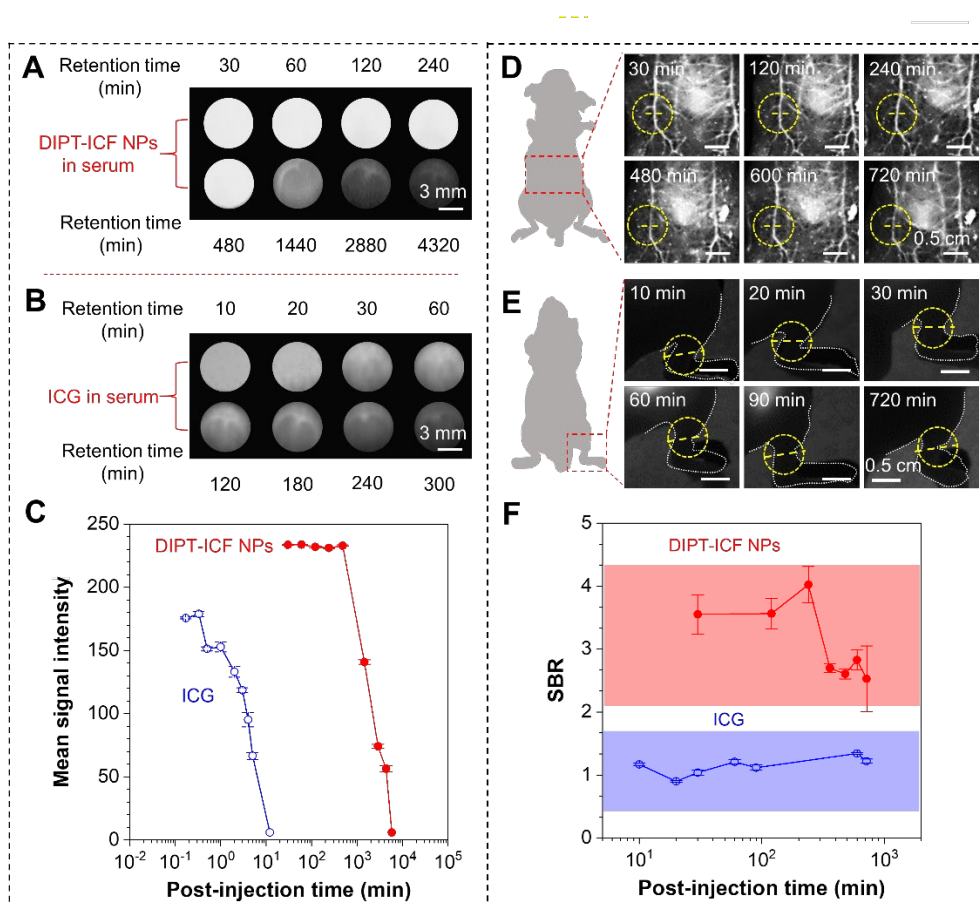

Fig. 3. Retention time of DIPT-ICF NPs and ICG in the blood circulation of mice. (**A**) NIR-II images of serum collected from mice's blood were captured at different time points (30, 60, 120, 240, 480, 1440, 2880, and 4320 min) post-injection of DIPT-ICF NPs through tail veins (980 nm laser, 60 mW/cm^2, 1319 nm LP, and exposure time 200 ms). (**B**) NIR-I images of serum collected from mice at different time points (10, 20, 30, 60, 120, 180, 240, and 300 min) post-injection of ICG via tail veins were captured (808 nm laser, 900 nm LP, and exposure time 30 ms). (**C**) The quantitative analysis curves of mean signal intensity of DIPT-ICF NPs and ICG in panel (A) and (B), respectively. (**D**) The NIR-II angiography was performed on abdominal vessels of mice at

different time points post-injection of DIPT-ICF NPs (980 nm laser, power density 60 mW/cm^2, 1319 nm LP, and exposure time 200 ms). (**E**) The NIR-I images were captured on mice at different time points after ICG injection (808 nm laser, 900 nm LP, and exposure time 35 ms). (**F**) The quantitative analysis of SBR in ROI regions marked with the yellow dashed lines and circles in (D) and (E).

circulation time of DIPT-ICF NPs is superior than that of ICG (Fig. 3C). The long-circulating capability of DIPT-ICF NPs in angiography was also confirmed. As shown in Fig. 3D and 3E, after 720 min post-injection of DIPT-ICF NPs, the abdominal vascular textures remained visible. In contrast, the fluorescent signals of ICG in the subcutaneous blood vessels rapidly disappear
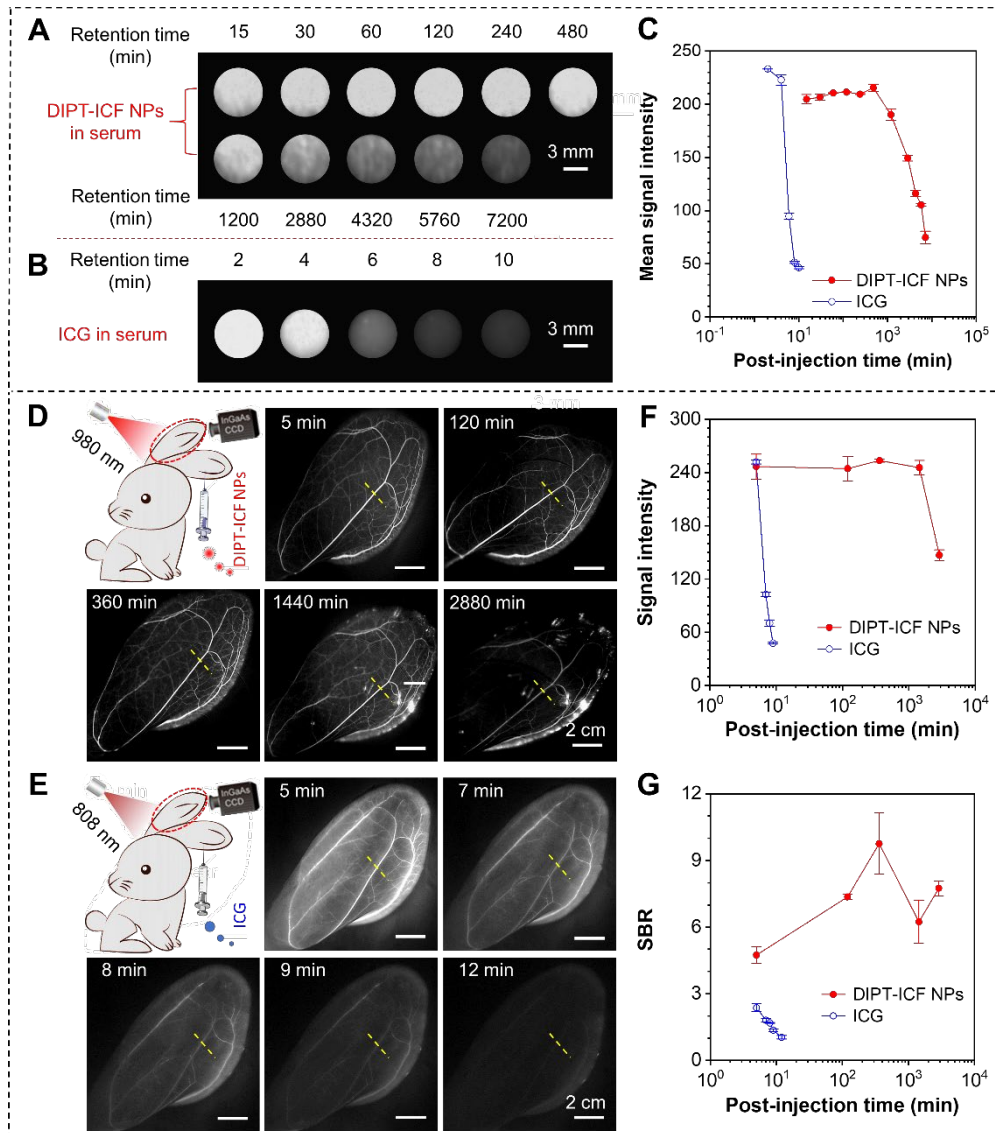

Fig. 4. Retention time of DIPT-ICF NPs and ICG in the blood circulation of rabbits. (**A**) NIR-II images of serum collected from rabbits at different time points (15, 30, 60, 120, 240, 480, 1200, 2880, 4320, 5760, and

7200 min) post-injection of DIPT-ICF NPs through ear veins were captured (980 nm laser, 60 mW/cm^2, 1319 nm LP, and exposure time 200 ms). (**B**) NIR-II images of serum collected from rabbits at different time points (0, 2, 4, 6, 8, and 10 min) post-injection of ICG. (**C**) The quantitative analysis curves of mean signal intensity of DIPT-ICF NPs in (A) and ICG in (B). (**D**) The NIR-II angiography was performed in rabbits' ears at 5, 120, 360, 2880, and 4320 min, after DIPT-ICF NPs injection. (**E**) The NIR-I angiography was performed in rabbits' ears at 5, 7, 8, 9, and 12 min after ICG injection. (**F**) The quantitative analysis curves indicated the signal intensity of DIPT-ICF NPs in the NIR-II window, and ICG in the NIR-I window. (**G**) Quantitative analysis indicated that NIR-II angiography in (D) using DIPT-ICF NPs as a fluorescence contrast agent, had a significantly higher SBR than that of NIR-I angiography in (E) using ICG.

which could not be observed after 10 min. The quantification of SBRs demonstrates the overwhelming advantage of DIPT-ICF NPs over ICG as a contrast agent for long-circulating angiography (Fig. 3F).

To further confirm the effectiveness of DIPT-ICF NPs in long-circulating angiography for big laboratory animals, circulating retention assessment of angiography were carried out in the rabbit models. The DIPT-ICF NPs was injected via the left ear marginal vein into the rabbits (0.3 mg/mL, 1.5 mg/kg), the serum sample was then collected at various time points to record the luminescence signal (Fig. 4, A and B). The circulating half-life time of DIPT-ICF NPs similarly is much longer than that of ICG in the rabbit blood circulation (4068 min vs 3.8 min, Fig. 4C). In vivo angiography experiment shows that stable and strong luminescence of DIPT-ICF NPs in ear vasculatures was observed clearly even over 2 days (Fig. 4D). While the signal of ICG rapidly disappear within 12 min (Fig. 4, E and F). Moreover, the SBR (defined as the vessel-signal-to-skin ratio) of DIPT-ICF NPs was significantly higher than that of ICG (Fig. 4G). The excellent performance of DIPT-ICF NPs inspire us to further explore its real application for intraoperative renal angiography and assessment of renal graft reperfusion in rabbit models.

Intraoperative renal angiography and assessment of renal graft reperfusion in rabbit models

The intraoperative precise anatomy of the donor's renal vasculatures and evaluation of renal allograft vascular patency post-reconstruction are highly significant for the success of renal transplantation. To evaluate the performance of DIPT-ICF NPs in fluorescence angiography of the donor renal vasculatures, donor nephrectomy and renal graft vasculature reconstruction models were successfully established to simulate real clinical scenarios. As shown in Fig. 5A, the distribution of renal artery and vein of the donor kidney as well as the blood patency rate were

firstly evaluated with DIPT-ICF NPs before the renal transplantation. At 36 s after injection of DIPT-ICF NPs, the renal artery was visualized first, and the contour of the kidney and renal vein then emerged and gradually became sharper, becoming highly bright at a time of 95 s. The high-resolution renal angiography revealed that the kidney of the donor rabbit had a single renal vein and renal artery, which had no malformation. The relationship of post-injection time and fluorescence signal intensity further suggested that the blood entered the kidney from the renal artery off the abdominal aorta and left via the renal vein to the inferior vena cava (Fig. 5B). Next, renal graft angiography and reperfusion imaging based on DIPT-ICF NPs were performed in the
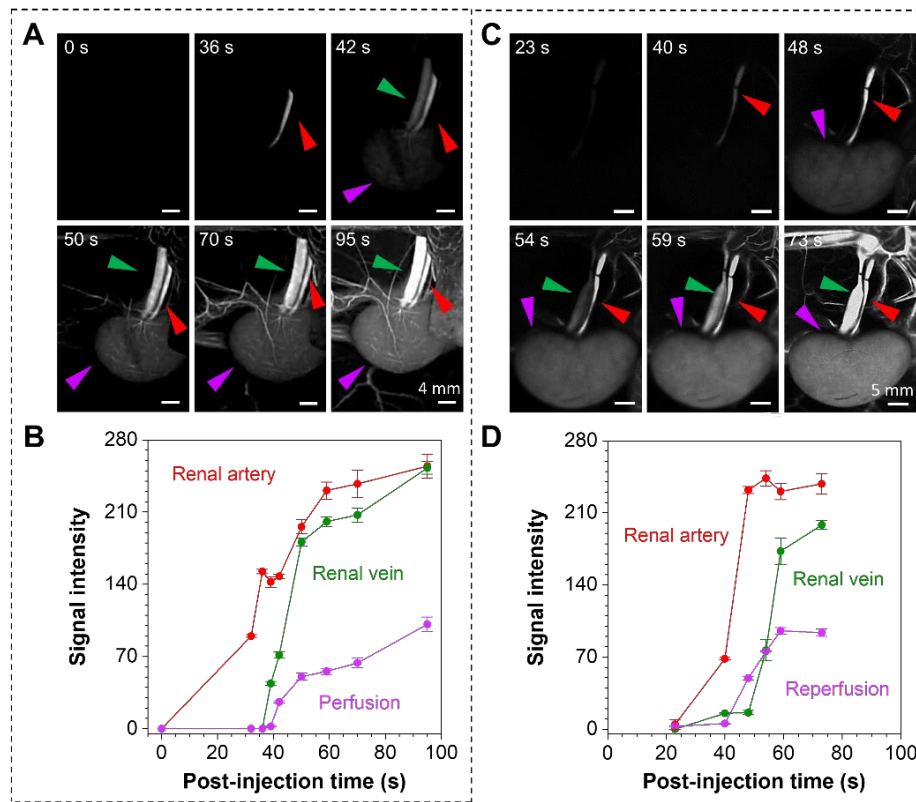

Fig. 5. Donor renal angiography, renal perfusion imaging, and reperfusion imaging on renal grafts were performed before and after kidney transplantation in the NIR-II window. (**A**) NIR-II images of the renal artery, the renal vein, and the kidney perfusion were captured at different time points by injecting DIPT-ICF NPs via the rabbit ear vein. Red arrows, green arrows, and yellow arrows represent renal artery, renal vein, and renal perfusion. After the NIR-II contrast agent injection, the renal artery and vein were lighted up at 32 s and 39 s, respectively. The time of kidney outline presentation was 42 s after contrast agent injection. (**B**) Quantitative analysis of NIR-II fluorescence Intensity of kidney and its blood vessels was conducted in (A). (**C**) NIR-II images of the graft artery, the graft vein, and the graft reperfusion following renal vascular anastomosis were acquired at different time points by injecting DIPT-ICF NPs through the rabbit ear vein. During kidney

transplantation, the renal graft artery, vein, and the renal graft reperfusion could be visualized in real-time with high resolution, and the patency of anastomosis of graft vascular could be observed by NIR-II imaging. (**D**) Quantitative analysis of NIR-II fluorescence intensity of the renal graft artery, the renal graft vein, and the renal graft reperfusion was conducted in (C). All NIR-II images were taken with the 980 nm laser at a power density of 60 mW/cm^2, long pass 1319 nm filter, and exposure time of 200 ms.

orthotopic renal transplantation of rabbits to assess the blood patency rate after revascularization. As shown in Fig. 5C, the reconstructed graft artery and vein were visualized sequentially from 40 s to 54 s after intravenous injection of DIPT-ICF NPs. Furthermore, the luminescence signal was uniformly distributed on the grafted renal, suggesting a good blood patency rate and blood perfusion of the kidney after revascularization. Quantitative analyses of the reconstructed graft artery and vein showed that the NIR-II fluorescent signal in the renal artery, vein, and renal graft exhibited similar changing tendency as those of donor renal before the transplantation, further suggesting the successful vascular anastomosis during the renal transplantation (Fig. 5D). It is worthy to note that due to the high brightness and deep penetration depth of DIPT-ICF NPs, the renal vein covered by soft tissues could even be differentiated easily and distinctly. This benefits the accurate ligation and severance of the veins in donor nephrectomy, which avoids the massive hemorrhage in a living-donor and helps improve the kidney preparation efficiency in advance of the transplant procedure. As shown in Fig. S9, one small vein (around 1.0 mm in diameter) and cranial abdominal vein (*38*) (2.5-3.0 mm in diameter), the two branches of the left renal vein could be easily and effectively ligated and severed using the image-guided donor nephrectomy. These results show the feasibility of DIPT-ICF NPs assisted NIR-II renal angiography in guiding the kidney transplants, which could be used by the surgeons to make timely management.

NIR-IIa angiography for diagnosing vascular complications and assessing renal reperfusion in rabbit Kidney transplantation models

Vascular anastomotic stenosis is a common complication that could directly cause hypoperfusion of the allograft and lead to delayed graft function, which however is hardly identified with naked eyes (Fig. 6a) (*39*). Three types of anastomotic stenosis models in orthotopic renal transplantation are established to evaluate the feasibility of DIPT-ICF NPs for rapidly diagnosing abnormal anastomosis of graft vasculatures. DIPT-ICF NPs were intravenously administrated into the rabbit models and then the stenosis of the vascular after anastomosis was evaluated. As shown in Fig. 6B, the control kidney without any stenosis showed bright artery and vein and uniform

fluorescence distribution. However, for kidney with complete stenosis of the graft artery, no fluorescence signal could be detected, suggesting the function loss of graft artery. For kidney with partial stenosis of the graft artery, only few blood vessels could be light up by the NIR-II fluorescence due to artery blood vessel dysfunction. It is worthy to note that complete blockage of renal veins could also cause the blood insufficient of graft kidney although not so severe as artery dysfunction. Further quantitative analyses of the fluorescence signal intensity obtained from the reconstructed renal vessels and renal graft confirmed that the abnormal vascular anastomosis was accompanied by poor renal reperfusion (Fig. 6C; S10).
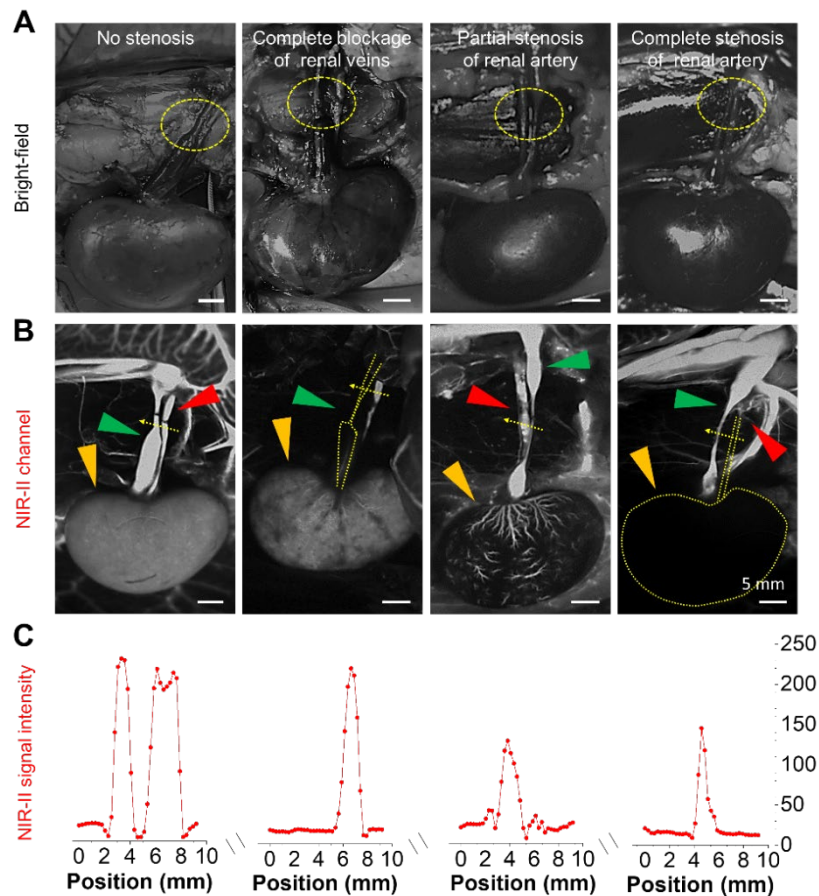

Fig. 6. Application of NIR-II imaging to monitor the vascular anastomosis of the renal graft in real-time during orthotopic kidney transplantation. (**A**) The bright-field images were captured in different types of vascular anastomotic abnormalities (no stenosis, complete stenosis of renal veins, partial stenosis of renal artery, and complete stenosis of renal artery) when kidney transplantation was processed. (**B**) The NIR-II images of different vascular anastomotic abnormalities corresponded to the bright field images in (A). (**C**) NIR-II fluorescence intensity measurement of the cross-sectional profile along the yellowed dashed lines in (B). The yellow dashed circles in (A) indicate renal vascular anastomosis. The red, green, and orange arrows in (B)

represent the arteries, veins, and blood reperfusion of renal grafts. All NIR-II images were captured with a 980 nm laser at the power density of 60 mW/cm^2, 1319 nm LP, and an exposure time of 200 ms.

Next, to simulate the scene of vascular anastomosis more realistically in kidney transplantation, the heterotopic kidney transplant models of rabbits were established. Prior to the donor kidney implantation, the iliac vessels were identified and assessed regarding suitability for anastomosis. Based on the bright field images (Fig. S11A), it is hard to distinguish the iliac vessels and their branches from the complex vascular network against the blood-red background. Iatrogenic obturator nerve injury and serious complications would be resulted if iliac vasculatures could not be separated with precise location during the operation. Fortunately, post intravenous injection of DIPT-ICF NPs immediately light up the iliac blood vessels including iliac arteries, common iliac veins, and vascular branches of the postcava and abdominal aorta with high resolution in the NIR-IIa channel (Fig. S11A). After the anatomy of the iliac vessels was clearly demonstrated, ectopic renal implantation was carried out with end-to-side anastomosis of the renal artery and common iliac artery, and end-to-end anastomosis of the renal vein and common iliac vein (*7*). As shown in Fig. S11B, the patency of vascular anastomosis and reperfusion of the renal allograft could be clearly displayed. In general, abnormal anastomosis of graft vasculatures and the resulted poor renal allograft reperfusion could be easily diagnosed by DIPT-ICF NPs based angiography.

Ureterovesical junction imaging of kidney transplantation in the NIR-IIa window

Performing ureterovesical anastomosis in kidney transplantation is another main step in the surgery (*40*). However, surgical error and ureteral ischemia resulted necrosis will cause the occurrence of ureteral complications such as urinary leakage (incidence of ~9.3%) and ureteral stenosis (incidence of ~10.5%) at the site of the ureteral junction, which threaten the graft function (*41, 42*). The excellent in vivo imaging capability of DIPT-ICF NPs enables its application in diagnosis of ureteral complications caused by anastomotic failure. With injecting DIPT-ICF NPs (0.1 mg/mL, dispersed in PBS solution) into the ureter anterogradely via the renal pelvis (Fig. 7A), the ureter and bladder were immediately illuminated. As shown in Fig. 7B, there was no urinary leakage or obstruction in the anastomotic site in the successful anastomosis model, and the bladder could be successfully light up. However, for the obstruction model of ureterovesical anastomosis, the obstruction prevents recipient's bladder being filled with the DIPT-ICF NPs and leads to the lack of fluorescent signal inferior to the anastomotic site of the ureter and bladder (Fig. 7C). Moreover, the bright fluorescence signal around recipient's bladder indicates that the leakage of

urine from the ureterovesical suturing site (Fig. 7D). Quantitative analysis showed that the mean fluorescence intensity of the recipient's bladder in either the urinary leak or ureteral stenosis model was significantly reduced in contrast to the successful urinary tract reconstruction model, suggesting that the urine excreted by the donor kidney could not flow unimpeded into the bladder (Fig. 7E). Collectively, these results demonstrate the capability of DIPT-ICF NPs as an excellent contrast agent for fluorescent ureterography in the NIR-IIa window.
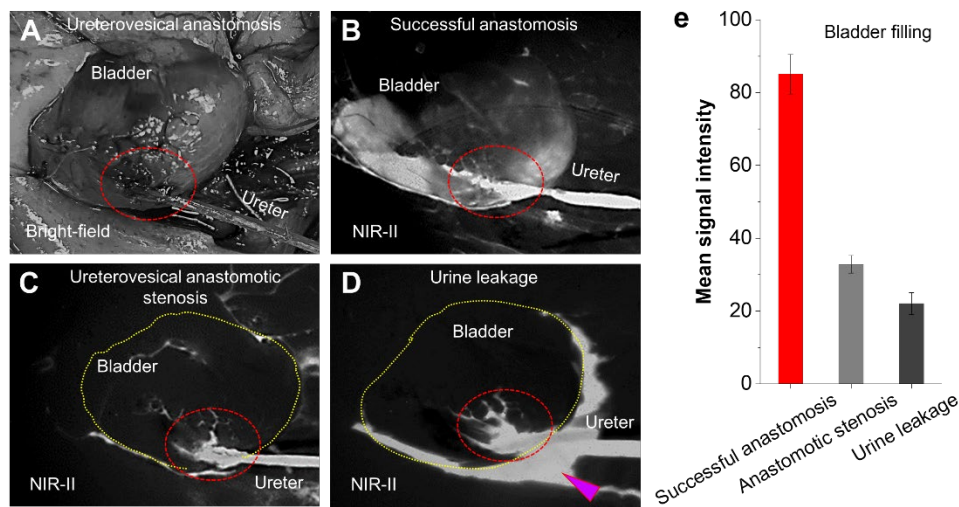

Fig. 7. NIR-IIa anterograde ureterography in renal transplantation based on DIPT-ICF NPs. (**A**) The bright-field and (**B**) NIR-II fluorescence images of successful ureterovesical anastomosis. Fluorescence images of ureterovesical anastomotic abnormalities, such as (**C**) ureterovesical anastomotic stricture and (**D**) urine leakage using DIPT-ICF NPs in the NIR-II window. (E) Measurements of NIR-II fluorescence signal intensity in (B), (C), and (D), respectively. The red dashed circles indicate the ureterovesical anastomosis sites. The purple arrow in (D) represents poor ureterovesical anastomosis, resulting in urine leakage. All NIR-II images were captured with a 980 nm laser at the power density of 60 mW/cm^2 with the 1319 nm LP, and an exposure time of 200 ms.

Discussion

Good donor kidney quality is the basis for long-term graft survival (*43*). A rapid and noninvasive assessment of donor kidney quality is necessary before implantation. As far as we know, utilizing NIR-II imaging technology to assess donor kidneys' quality before renal implantation has scarcely been reported. By flushing renal preservation fluids containing non-degradable hydrogel microspheres (200 and 500 μm in diameter) into the donor kidneys, two sorts of rabbit models were established to simulate the donor kidney with suboptimal conditions. As shown in Fig. S12,

after perfusing with DIPT-ICF NPs through the renal artery, the fluorescence signal can clearly present the embolism extent of intrarenal arteriole. For kidney without embolism, the fluorescence signal was uniformly distributed over the kidney surface without fluorescence signal defect area (Fig. S12, A and D). However, the fluorescence signal of embolized kidney exhibited alternately bright and dark regions on the renal surface (Fig. S12, B and E), in which the dark regions represented the ischemia areas caused by arteriole embolisms while the bright areas indicated good kidney perfusion without intrarenal embolisms. For kidney flushed by larger size of microspheres, most renal segment arteries were embolized, and more than 2/3 of the renal surface fluorescence signal was lost (Fig. S12, C and F). These results suggest the feasibility of NIR-IIa imaging based on DIPT-ICF NPs for detecting intrarenal embolism.

Donor kidneys may also experience various potential periods of ischemic injuries during kidney transplants despite continuous advances in surgical and hypothermic perfusion techniques (*44*). However, as shown in Fig. 8A, the change of the kidneys undergoing different degrees of warm ischemia could not be identified with the naked eyes. With the help of NIR-II fluorescence angiography technology, the discrepancies of kidneys upon different ischemia times could be rapidly identified (Fig. 8B). In general, normal kidney without ischemic injury showed uniformed fluorescence over the whole kidney after the injection of DIPT-ICF NPs from renal artery, while the fluorescence signal of the injured kidneys changed from uniformity to miliary distribution and show a decrease with different warm ischemia times (WITs) (Fig. 8, B and C). Periodic Acid-Schiff (PAS) staining (*45*) results indicated that in warm ischemia kidney models, the glomeruli volume decreased, accompanied by enlarged glomerular capsules and the corresponding renal tubular epithelial cells vacuolized, suggesting the lesion and necrosis of glomeruli and renal tubule (Fig. 8D). The ematoxylin and eosin (H&E) staining displayed that red blood cell trapping and congestion in renal microcirculation became more and more severe with the ischemia time, which induced the formation of microthrombus and caused the speckled distribution of fluorescence in the kidney (Fig. 8E). Additionally, the DIPT-ICF NPs were unable to pass through the glomerular filtration barrier (GFB) of normal kidneys (particle size of > 6 nm could not penetrate the GFB) (*46*), and were mainly excreted into the gut through the bile (Fig. S13), appearing in the feces (Fig.S14) rather than the urine (Fig. S15). As shown in the TEM images (Fig. 8F), the three layers of glomerular filtration barrier (GFB) including the glomerular endothelial cell (GEC), glomerular basement membrane (GBM), and podocyte foot processes (*47*) were damaged when suffering

warm ischemia, which lead to DIPT-ICF NPs crossing through the GFB and entering the urine (Fig. S16); thus, it is easily to identify GFB damages by urine fluorescence monitoring (Fig. 8G). Therefore, as an excellent fluorescence contrast agent, DIPT-ICF NPs can be applied to rapidly assess the reperfusion and function of renal grafts by monitoring NIR-II fluorescence on the surface of the kidney and in the urine.
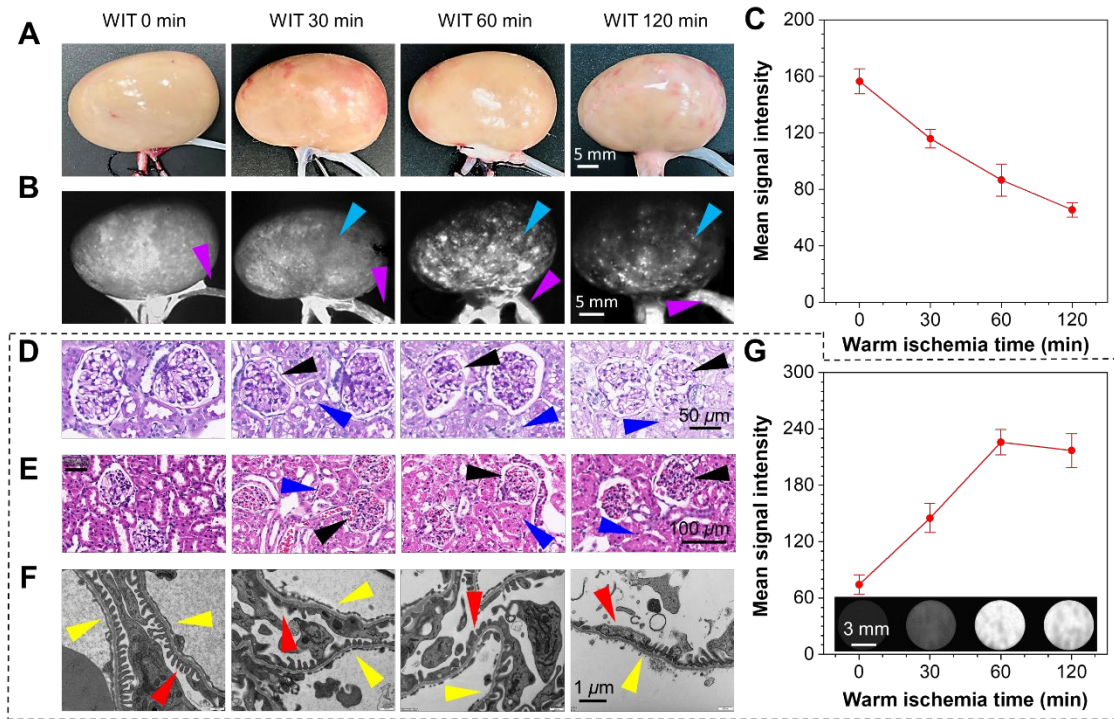

Fig. 8. The renal donor grafts with different warm ischemia duration (0, 30, 60, and 120 min) were perfused with PBS to flush out the blood, then contrast agent DIPT-ICF NPs infused via the renal artery into the kidney. (**A**) Color images and (**B**) NIR-II images of the donor's kidneys were captured after antegrade injection of DIPT-ICF NPs via the renal artery. (**C**) Quantitative analysis of NIR-II mean signal intensity of kidneys under different warm ischemia duration in (b). (**D**) Periodic Acid Schiff (PAS) and (**E**) Hematoxylin-eosin (HE) staining of the glomerulus from donor kidneys undergoing different warm ischemia times in (A). With the warm ischemia time increasing, the microvascular network in the glomerulus became degeneration and pyknosis, accompanied by the renal tubular epithelial cells degenerated and necrotic. (**F**) TEM images of the glomerular filtration barrier, of which the tissue was taken from the donor's kidneys undergoing warm ischemia times in (A), respectively. As the warm ischemia time increased, the damage to the three-layer structure of the glomerular basement membrane (GBM) was gradually aggravated, the foot process fusion of podocytes became more and more apparent, and the glomerular electron-dense layers became thinner and thinner. (**G**) Quantification of NIR-II mean intensity of the urine excreted from the ureters when the contrast agent DIPT-ICF NPs was infused into the donor rabbits' kidneys via the renal artery. The inset shows NIR-II images of the

urine excreted from the ureters during perfusion of DIPT-ICF NPs in donor rabbits' kidneys undergoing warm ischemia in (A). The black and blue arrows in (D) and (E) represented atrophied glomerulus and degenerated necrotic tubules due to warm ischemia, respectively; the red and yellow arrows in (F) indicate GBM rupture and glomerular epithelial cell foot process fusion, respectively. All NIR-II images were captured under a 980 nm laser (60 mW/cm^2) with a 1319 nm LP and an exposure time of 200 ms.

The biocompatibility and biosafety of DIPT-ICF NPs were evaluated. The cytotoxicity of the DIPT-ICF NPs on human cancer cell Hela and human fibroblast cell 3T3 was first assessed through cell counting kit-8 (CCK-8). As shown in Fig. S16, even though the concentration was increased to 500 µg/mL, the cell viability was not notably affected after 24 h incubation. Additionally, the toxicity of the DIPT-ICF NPs was evaluated through a histological investigation of organs in vivo. H&E staining demonstrated that no noticeable tissue damage and inflammatory lesion were caused in the vital organs of the mice and rabbits (Fig. S17). To further investigate the potential toxicology of DIPT-ICF NPs, healthy Balb/c nude mice and rabbits intravenously administrated with DIPT-ICF NPs (0.5 mg/mL based on DIPT-ICF) as well as untreated healthy mice and rabbits were received serum biochemistry assay and complete blood count after 14 days post injection. The liver function indicators, including alanine aminotransferase (ALT), aspartic acid transaminase (AST), blood urea nitrogen (BUN), and Serum creatinine (Scr) were all measured to be normal (Fig. S18A), revealing that no obvious hepatic and renal disorders for DIPT-ICF NPs-treated mice and rabbits. Besides, the assay of the blood panel, including white blood cells (WBC), hemoglobin (Hgb), red blood cells (RBC), as well as platelets (PLT), indicates that there are not statistical differences in these indicators between DIPT-ICF NPs and untreated groups (Fig. S18B). These results indicated that DIPT-ICF NPs was a highly biocompatible and biosafety contrast agent without noticeable side effects on living mice and rabbits, which benefits the translation of AIE NPs-assisted angiography and bioimaging for clinical applications.

In summary, a highly bright NIR-II luminescent nano-contrast agent based on an AIEgen DIPT-ICF has been rationally designed and prepared. Compared to ICG, DIPT-ICF nano contrast agent holds the merits of high brightness, superior photostability, long-circulating time, and excellent biocompatibility, which could fulfill the requirement of an ideal contrast agent in complex physiological environment for organ transplantation surgery. The results indicate that a single dose of DIPT-ICF NPs contrast agent could monitor the entire surgical process very clearly via luminescence due to its high brightness and long-circulating character. This is much better than

traditional luminescent contrast agent of ICG, whose luminescence brightness and circulating time are not sufficient to support the completion of a whole organ transplantation surgery. In living-donor nephrectomy, NIR-II angiography of renal vasculature based on DIPT-ICF NPs helps surgeons visualize the renal vascular branches and their anatomical location to avoid iatrogenic donor kidney injury. Meanwhile, the surgical complications in vascular and ureterovesical anastomosis can be observed in real-time by NIR-II angiography and ureterography using DIPT-ICF NPs as a contrast agent. Furthermore, GFB injury of the donor's kidney following warm ischemia and renal graft reperfusion could be evaluated through DIPT-ICF NPs based NIR-II imaging. The present study demonstrates a superior NIR-II nano contrast agent and its application in monitoring the whole process of organ transplantation surgery, which provides reliable and effective technical support for monitoring and evaluating renal transplantation in the clinic.

MATERIALS AND METHODS

Materials

All the chemicals and reagents were purchased from chemical sources, and the solvents for chemical reactions were distilled before use. All air and moisture sensitive reactions were carried out in flame-dried glassware under a nitrogen atmosphere. Pluronic® F-127 was bought from Sigma-Aldrich. ICG was bought from TCI. Cell Counting Kit-8 (CCK-8) was purchased from DoJindo. Dulbecco's modified Eagle's medium (DMEM), Fetal bovine serum (FBS), penicillin-streptomycin, phosphate-buffered saline (PBS), and trypsin were obtained from ThermoFisher.

Measurements

The UV-Vis-NIR absorption spectra were performed using a PerkinElmer Lambda 365 spectrophotometer. 1H and 13C spectra were recorded at room temperature on a Unity-400 NMR spectrometer using $CDCl_3$ as solvent and tetramethylsilane (TMS) as a reference. Photoluminescence (PL) measurement was performed using a Horiba FluoroMax-4 Spectrofluorometer. The size distribution and average size of the DIPT-ICF NPs were performed by DLS using a Zeta-plus potential analyzer. TEM images were captured by a FEI Tecnai F20 microscope (accelerating voltage of 200 kV). Density functional theory (DFT) calculations were carried out by the B3LYP/6G(d), Gaussian 09 package. All the NIR-II images were captured through Full spectrum in vivo fluorescence imaging system (Suzhou NIR-Optics Technology Co., Ltd.).

Assessment of quantum yield (Φ_{PL}) of the dyes of DIPT-IC, DIPT-ICF and DIPT-ICF NPs

The Φ_{PL} of DIPT-IC, DIPT-ICF and DIPT-ICF NPs was determined like the way of the previous literature, using NIR-II fluorescent IR-26 dye as the reference ($\Phi_{PL} = 0.5\%$) (*48*). For reference calibration, IR-26 dissolved in 1,2dichloroethane (DCE) was diluted to a DCE solution to prepare five samples with their absorbance value at 808 nm of ~0.1, ~0.08, ~0.06, ~0.04, and ~0.02. Then a total of five IR-26 solutions in DCE with linearly spaced concentrations were transferred into 10-mm path fluorescence cuvette at a time. the excitation source was an 808 nm diode laser. The emission was collected in the transmission geometry with a 1000 nm long-pass filter to reject the excitation light and emission spectrum was taken in the 1000 to 1500 nm region. Then all emission spectra of both the reference and the samples were integrated into the 1000 to 1500 nm NIR-II region. The integrated NIR-II fluorescence intensity was plotted against absorbance at the excitation wavelength of 808 nm and fitted into a linear function. The slopes, obtained from the reference of IR-26 in DCE and the other from the sample, were employed in the calculation of the quantum yield of the sample, based on the equation as follows $\Phi_{PL,sample} = \Phi_{PL,ref} \cdot \frac{Slope_{sample}}{Slope_{ref}} \cdot$

$\left(\frac{n_{sample}}{n_{ref}} \right)^2$

where n_{sample} and n_{ref} represent the refractive indices of H_2O and DCE, respectively.

Cell culture

HeLa cells and NIH/3T3 cells were cultured in the DMEM containing 10% FBS and 1% penicillin-streptomycin (100 units/mL penicillin and 100 g/mL streptomycin) in a 5% CO_2 humidity incubator at 37 °C.

Cytotoxicity study of DIPT-ICF NPs

CCK-8 assays were employed to evaluate the cytotoxicity of DIPT-ICF NPs against HeLa cells and NIH/3T3 cells. In brief, HeLa and NIH/3T3 cells were incubated in 96-well plates (Sarsteadt AG & Co. KG., Germany) at a density of 1×10^5 cells/mL. Post 24 h incubation, the cells were exposed to a various of doses of DIPT-ICF NPs. At 24 h post addition of DIPT-ICF NPs, the wells were washed with PBS (1×, pH 7.4) buffer and 100 μL freshly prepared medium containing CCK-8 solution (the volume ratio of CCK-8 was 10%) was added into each well, then the cells were kept in the incubator for 1.5 hours. Cell viability was expressed by the ratio of the absorbance of cells incubated with NPs to that of the cells incubated with culture medium only.

Animal experiments

The BALB/c mice and New Zealand rabbits were purchased from the Guangdong Medical Laboratory Animal Center. The *in vivo* experiments were carried out with permission from the Guidance Suggestions for the Care and Use of Laboratory Animals. All procedures were approved by the Chinese University of Hong Kong (Shenzhen) (CUHKSZ) and Southern University of Science and Technology (SUSTech) Animal Care and Use Committees.

Kidney transplantation

New Zealand rabbits weighing 2.5-3.0 kg were used for establishing orthotopic and ectopic kidney transplantation models.

Anesthesia: Initially, the surgical anesthesia was induced by chloral hydrate (3% w/v) (Merck & Co., Inc.) and Xylazine (3% w/v) (Merck & Co., Inc.) solution through subcutaneous injection. After 15 min, the rabbits were anesthetized with continuous inhaling the mixture of isoflurane (RWD Life Science Co., Ltd.) and oxygen. During anesthesia, normal saline (NS) and glucose solution (5%) were used to maintain blood pressure and replenish energy of rabbit models. The cardiorespiratory monitor (RM500, RWD Life Science Co., Ltd.) was used to measure the heart rates, respiratory rates, and oxyhemoglobin saturation of rabbits for real-time adjustment of isoflurane inhalation volume. Using this method, rabbits could safely be held in the anesthetic state for 6-8 hours without mechanical ventilation. Before nephrectomy the model rabbits were injected intravenously with 500 units heparin for systemic heparinization to avoid thrombosis.

Donor kidneys retrieval: An abdominal midline incision (from the xiphoid process to the symphysis) was employed in nephrectomy (*49*). Before isolation of the left kidney, 2 mL of hydrochloride lignocaine (0.5%) was injected around the renal vessels to prevent the renal artery spasm produced by dissection. Then the peritoneum over the left kidney, vessels, and ureter was carefully divided, and the renal vessels and ureter were isolated along their full length. 26 G venous catheters were inserted into the proximal end of the renal artery and vein, which were fixed on the vessels. Immediately after the fixation of the catheters, the preservation fluid (4°C) was perfused into the left kidney through its artery until the fluid from the left renal vein became clear. Subsequently, the renal artery and the vein were clamped, divided, and ligated, and the kidney removed. The donor kidneys were preserved in cold preservation fluid (4°C).

Revascularization: For orthotopic kidney transplantation models, midline incisions were used in the recipient rabbits. Notably, to avoid constriction of mesenteric vasculature and possible development of hypotension and shock, the intestines should keep on the same levels with the edge

of the wound. The vascular anastomosis was performed with end-to-end suture. For ectopic kidney transplantation models, lower abdominal midline incisions were adopted in the recipient rabbits. The common iliac artery and common iliac vein were carefully divided. After completely exposing the common iliac vessels, the blood flow of the donor kidneys was reconstructed by means of end-to-side anastomosis. In revascularization processes of orthotopic and ectopic kidney transplantation, the surgery field was magnified by an operating microscope (magnification × 6). The anastomosis was performed with a continuous, atraumatic 8-0 silk suture.

Ureteral reconstruction (Ureteroneocystostomy): Extravesical ureteroneocystostomy was carried out after the donor kidney was perfused with recipient blood and hemostasis has been secured (*50*). Firstly, a longitudinal oblique incision was made for approximately 0.5 cm until the bladder mucosa bulges into the incision. Then the bladder mucosa was incised, and 6-0 monofilament absorbable sutures placed through both ends of the incision. The ureter distal end was brought to the mucosa incision, and the mucosal sutures passed through the two sides of the distal end, and the ureter parachuted on to the bladder. The ureter was anastomosed to the bladder mucosa with continuous sutures between the ureter and the mucosa of the bladder. While the ureteric anastomosis was complete, the seromuscular layer was closed over the ureter with interrupted absorbable sutures.

NIR-II fluorescence angiography in rabbits with intravenous injection of DIPT-ICF NPs

The models of New Zealand rabbits were used for NIR-II fluorescence angiography of the vasculatures with the intravenous injection of DIPT-ICF NPs (0.3 mg/mL, 1.5 mg/kg).

Ear angiography: The rabbits were anesthetized with the method described above and fixed properly. Clip the fur from the left rabbit ears and further remove the hair with a depilatory cream. The fluorescence contrast agent DIPT-ICF NPs (0.3 mg/mL, 1.5 mg/kg) or ICG (0.05 mg/mL, 200 μL) was injected through the right ear marginal vein, followed by ear angiography at various time points.

Kidney angiography: The rabbits were anesthetized with the method described above and fixed properly. An abdominal midline incision (from the xiphoid process to the symphysis) was employed to exposure the kidney and its accessory vessels. DIPT-ICF NPs (0.3 mg/mL, 1.5 mg/kg) was injected through the ear marginal vein of each rabbit models, then NIR-II imaging were performed.

NIR-II fluorescence ureterography in rabbits with intraureteral injection of DIPT-ICF NPs

After the completion of the ureteroneocystostomy anastomosis, the contrast medium DIPT-ICF NPs (0.1 mg/mL) was injected antegrade into the ureter through the renal graft pelvis, and NIR-II imaging of the vesicoureteral anastomosis was performed.

Statistical analysis

Quantitative data were expressed as mean ± standard deviation. Statistical comparisons were made by ANOVA analysis and Student's t-test. *P* value < 0.05 was considered statistically significant.

References and Notes

1. R. Boissier, V. Hevia, H. M. Bruins, K. Budde, A. Figueiredo, E. Lledo-Garcia, J. Olsburgh, H. Regele, C. F. Taylor, R. H. Zakri, C. Y. Yuan, A. Breda, The Risk of Tumour Recurrence in Patients Undergoing Renal Transplantation for End-stage Renal Disease after Previous Treatment for a Urological Cancer: A Systematic Review. *Eur Urol* **73**, 94-108 (2018).
2. E. Ok, G. Asci, C. Chazot, M. Ozkahya, E. J. Mees, Controversies and problems of volume control and hypertension in haemodialysis. *Lancet* **388**, 285-293 (2016).
3. C. O. T. D. Foundation, Report on the Development of Organ Transplantation in China (2020).
4. P. J. Held, F. McCormick, A. Ojo, J. P. Roberts, A Cost-Benefit Analysis of Government Compensation of Kidney Donors. *Am J Transplant* **16**, 877-885 (2016).
5. C. Liu, I. E. Hall, S. Mansour, H. R. Thiessen Philbrook, Y. Jia, C. R. Parikh, Association of Deceased Donor Acute Kidney Injury With Recipient Graft Survival. *JAMA Netw Open* **3**, e1918634 (2020).
6. S. Hariharan, A. K. Israni, G. Danovitch, Long-Term Survival after Kidney Transplantation. *N Engl J Med* **385**, 729-743 (2021).
7. C. J. E. Watson, P. J. Friend, L. P. Marson, in *Kidney Transplantation - Principles and Practice (Eighth Edition),* S. J. Knechtle, L. P. Marson, P. J. Morris, Eds. (Elsevier, Philadelphia, 2019), pp. 157-172.
8. D. Dimitroulis, J. Bokos, G. Zavos, N. Nikiteas, N. P. Karidis, P. Katsaronis, A. Kostakis, Vascular complications in renal transplantation: a single-center experience in 1367 renal transplantations and review of the literature. *Transplant Proc* **41**, 1609-1614 (2009).
9. A. L. H. Gerken, K. Nowak, A. Meyer, M. C. Kriegmair, C. Weiss, B. K. Kramer, P. Glossner, K. Heller, I. Karampinis, F. Kunath, N. N. Rahbari, K. Schwenke, C. Reissfelder, W. Lang, U. Rother, Ureterovesical Anastomosis Complications in Kidney Transplantation: Definition, Risk Factor Analysis, and Prediction by Quantitative Fluorescence Angiography with Indocyanine Green. *J Clin Med* **11**, (2022).
10. M. A. Mickelson, R. J. Hardie, A. M. Hespel, J. Dreyfus, Evaluation of a microvascular anastomotic coupler for end-to-side arterial and venous anastomosis for feline renal transplantation. *Vet Surg* **50**, 213-222 (2021).
11. I. Expert Panel on Urologic, M. T. Taffel, P. Nikolaidis, M. D. Beland, M. D. Blaufox, V. S. Dogra, S. Goldfarb, J. L. Gore, H. J. Harvin, M. E. Heilbrun, M. T. Heller, G. Khatri, G. M. Preminger, A. S. Purysko, A. D. Smith, Z. J. Wang, R. M. Weinfeld, J. J. Wong-You-Cheong, E. M. Remer, M. E. Lockhart, ACR Appropriateness Criteria((R)) Renal Transplant Dysfunction. *J Am Coll Radiol* **14**, S272-S281 (2017).

12. J. Arevalo Perez, F. Gragera Torres, A. Marin Toribio, L. Koren Fernandez, C. Hayoun, I. Daimiel Naranjo, Angio CT assessment of anatomical variants in renal vasculature: its importance in the living donor. *Insights Imaging* **4**, 199-211 (2013).

13. M. Onniboni, M. De Filippo, R. Averna, L. Coco, M. Zompatori, N. Sverzellati, C. Rossi, Magnetic resonance imaging in the complications of kidney transplantation. *Radiol Med* **118**, 837-850 (2013).

14. D. Theerakulpisut, B. Thinkhamrop, S. Anutrakulchai, Comparison between Tc-99 m DTPA and Tc-99 m MAG3 Renal Scintigraphy for Prediction of Early Adverse Outcome After Kidney Transplantation. *Nucl Med Mol Imaging* **55**, 302-310 (2021).

15. J. Huang, K. Pu, Near-infrared fluorescent molecular probes for imaging and diagnosis of nephro-urological diseases. *Chem Sci* **12**, 3379-3392 (2020).

16. G. Hong, S. Diao, J. Chang, A. L. Antaris, C. Chen, B. Zhang, S. Zhao, D. N. Atochin, P. L. Huang, K. I. Andreasson, C. J. Kuo, H. Dai, Through-skull fluorescence imaging of the brain in a new near-infrared window. *Nat Photonics* **8**, 723-730 (2014).

17. A. L. Vahrmeijer, M. Hutteman, J. R. van der Vorst, C. J. van de Velde, J. V. Frangioni, Image-guided cancer surgery using near-infrared fluorescence. *Nat Rev Clin Oncol* **10**, 507-518 (2013).

18. R. R. Zhang, A. B. Schroeder, J. J. Grudzinski, E. L. Rosenthal, J. M. Warram, A. N. Pinchuk, K. W. Eliceiri, J. S. Kuo, J. P. Weichert, Beyond the margins: real-time detection of cancer using targeted fluorophores. *Nat Rev Clin Oncol* **14**, 347-364 (2017).

19. S. Zhu, R. Tian, A. L. Antaris, X. Chen, H. Dai, Near-Infrared-II Molecular Dyes for Cancer Imaging and Surgery. *Adv Mater* **31**, e1900321 (2019).

20. X. Wang, Z. Jiang, Z. Liang, T. Wang, Y. Chen, Z. J. S. A. Liu, Discovery of BODIPY J-aggregates with absorption maxima beyond 1200 nm for biophotonics. *Sci Adv* **8**, eadd5660 (2022).

21. Y. Chen, S. Wang, F. Zhang, Near-infrared luminescence high-contrast in vivo biomedical imaging. *Nature Reviews Bioengineering* **1**, 60-78 (2023).

22. J. Qi, C. Chen, D. Ding, B. Z. Tang, Aggregation-Induced Emission Luminogens: Union Is Strength, Gathering Illuminates Healthcare. *Advanced Healthcare Materials* **7**, (2018).

23. L. Boni, G. David, A. Mangano, G. Dionigi, S. Rausei, S. Spampatti, E. Cassinotti, A. Fingerhut, Clinical applications of indocyanine green (ICG) enhanced fluorescence in laparoscopic surgery. *Surg Endosc* **29**, 2046-2055 (2015).

24. R. Tian, Q. Zeng, S. Zhu, J. Lau, S. Chandra, R. Ertsey, K. S. Hettie, T. Teraphongphom, Z. Hu, G. Niu, D. O. Kiesewetter, H. Sun, X. Zhang, A. L. Antaris, B. R. Brooks, X. Chen, Albumin-chaperoned cyanine dye yields superbright NIR-II fluorophore with enhanced pharmacokinetics. *Sci Adv* **5**, eaaw0672 (2019).

25. T. Iijima, Y. Iwao, H. Sankawa, Circulating blood volume measured by pulse dye-densitometry: comparison with (131)I-HSA analysis. *Anesthesiology* **89**, 1329-1335 (1998).

26. P. Modi, J. Rizvi, B. Pal, R. Bharadwaj, P. Trivedi, A. Trivedi, K. Patel, K. Shah, J. Vyas, S. Sharma, K. Shah, R. Chauhan, H. Trivedi, Laparoscopic kidney transplantation: an initial experience. *Am J Transplant* **11**, 1320-1324 (2011).

27. W. He, Z. Zhang, Y. Luo, R. T. K. Kwok, Z. Zhao, B. Z. Tang, Recent advances of aggregation-induced emission materials for fluorescence image-guided surgery. *Biomaterials* **288**, 121709 (2022).

28. S. J. Lim, M. U. Zahid, P. Le, L. Ma, D. Entenberg, A. S. Harney, J. Condeelis, A. M. Smith, Brightness-equalized quantum dots. *Nat Commun* **6**, 8210 (2015).

29. S. Liu, H. Ou, Y. Li, H. Zhang, J. Liu, X. Lu, R. T. K. Kwok, J. W. Y. Lam, D. Ding, B. Z. Tang, Planar and Twisted Molecular Structure Leads to the High Brightness of Semiconducting Polymer Nanoparticles for NIR-IIa Fluorescence Imaging. *J Am Chem Soc* **142**, 15146-15156 (2020).

30. J. Wang, P. Xue, Y. Jiang, Y. Huo, X. Zhan, The principles, design and applications of fused-ring electron acceptors. *Nat Rev Chem* **6**, 614-634 (2022).

31. G. Deng, P. Yin, X. Zeng, G. Wang, J. Liang, C. Cui, P. Shen, Effects of the length and steric hindrance of π-bridge on molecular configuration and optoelectronic properties of diindole[3,2-b:4,5-b′]pyrrole-based small molecules. *Dyes and Pigments* **171**, (2019).

32. S. Xu, Y. Yuan, X. Cai, C.-J. Zhang, F. Hu, J. Liang, G. Zhang, D. Zhang, B. J. C. S. Liu, Tuning the singlet-triplet energy gap: a unique approach to efficient photosensitizers with aggregation-induced emission (AIE) characteristics. *Chem Sci* **6**, 5824-5830 (2015).,

33. J. Mu, M. Xiao, Y. Shi, X. Geng, H. Li, Y. Yin, X. Chen, The Chemistry of Organic Contrast Agents in the NIR-II Window. *Angew Chem Int Ed* **61**, e202114722 (2022).

34. A. L. Antaris, H. Chen, K. Cheng, Y. Sun, G. Hong, C. Qu, S. Diao, Z. Deng, X. Hu, B. Zhang, X. Zhang, O. K. Yaghi, Z. R. Alamparambil, X. Hong, Z. Cheng, H. Dai, A small-molecule dye for NIR-II imaging. *Nat Mater* **15**, 235-242 (2016).

35. J. Du, S. Liu, P. Zhang, H. Liu, Y. Li, W. He, C. Li, J. H. Chau, R. T. Kwok, J. W. Lam, Highly stable and bright NIR-II AIE dots for intraoperative identification of ureter. *ACS Appl. Mater. Interfaces* **12**, 8040-8049 (2020).

36. E. D. Cosco, A. L. Spearman, S. Ramakrishnan, J. G. P. Lingg, M. Saccomano, M. Pengshung, B. A. Arus, K. C. Y. Wong, S. Glasl, V. Ntziachristos, M. Warmer, R. R. McLaughlin, O. T. Bruns, E. M. Sletten, Shortwave infrared polymethine fluorophores matched to excitation lasers enable non-invasive, multicolour in vivo imaging in real time. *Nat Chem* **12**, 1123-1130 (2020).

37. Z. Hu, C. Fang, B. Li, Z. Zhang, C. Cao, M. Cai, S. Su, X. Sun, X. Shi, C. Li, T. Zhou, Y. Zhang, C. Chi, P. He, X. Xia, Y. Chen, S. S. Gambhir, Z. Cheng, J. Tian, First-in-human liver-tumour surgery guided by multispectral fluorescence imaging in the visible and near-infrared-I/II windows. *Nat Biomed Eng* **4**, 259-271 (2020).

38. P. Supuka, D. Mazensky, J. Danko, A. Supukova, E. Petrovova, Anatomical description of the renal arteries and veins in the European rabbit. *Biologia* **69**, 1059-1064 (2014).

39. U. Rother, K. Amann, W. Adler, N. Nawroth, I. Karampinis, M. Keese, S. Manap, S. Regus, A. Meyer, S. Porubsky, K. Hilgers, B. K. Kramer, W. Lang, K. Nowak, A. L. H. Gerken, Quantitative assessment of microperfusion by indocyanine green angiography in kidney transplantation resembles chronic morphological changes in kidney specimens. *Microcirculation* **26**, e12529 (2019).

40. A. Gallioli, A. Territo, R. Boissier, R. Campi, G. Vignolini, M. Musquera, A. Alcaraz, K. Decaestecker, V. Tugcu, D. Vanacore, S. Serni, A. Breda, Learning Curve in Robot-assisted Kidney Transplantation: Results from the European Robotic Urological Society Working Group. *Eur Urol* **78**, 239-247 (2020).

41. O. R. Faba, R. Boissier, K. Budde, A. Figueiredo, C. F. Taylor, V. Hevia, E. L. García, H. Regele, R. H. Zakri, J. J. E. u. f. Olsburgh, European Association of Urology guidelines on renal transplantation: update 2018. *Eur Urol Focus* **4**, 208-215 (2018).

42. A. J. Black, D. Harriman, C. J. C. U. A. J. Nguan, Contemporary risk factors for ureteral stricture following renal transplantation. *Can Urol Assoc J* **16**, (2022).

43. C. L. Davis, F. L. Delmonico, Living-donor kidney transplantation: a review of the current

practices for the live donor. *J Am Soc Nephrol* **16**, 2098-2110 (2005).

44. A. J. Vinson, C. Rose, B. A. Kiberd, A. Odutayo, S. J. Kim, I. Alwayn, K. K. Tennankore, Factors Associated With Prolonged Warm Ischemia Time Among Deceased Donor Kidney Transplant Recipients. *Transplant Direct* **4**, e342 (2018).

45. K. de Haan, Y. Zhang, J. E. Zuckerman, T. Liu, A. E. Sisk, M. F. P. Diaz, K. Y. Jen, A. Nobori, S. Liou, S. Zhang, R. Riahi, Y. Rivenson, W. D. Wallace, A. Ozcan, Deep learning-based transformation of H&E stained tissues into special stains. *Nat Commun* **12**, 4884 (2021).

46. M. J. Moeller, A. Chia-Gil, A step forward in understanding glomerular filtration. *Nat Rev Nephrol* **16**, 431-432 (2020).

47. I. S. Daehn, J. S. Duffield, The glomerular filtration barrier: a structural target for novel kidney therapies. *Nat Rev Drug Discov* **20**, 770-788 (2021).

48. A. T. R. Williams, S. A. Winfield, J. N. J. A. Miller, Relative fluorescence quantum yields using a computer-controlled luminescence spectrometer. *Analyst* **108**, 1067-1071 (1983).

49. I. A. Jacobsen, Renal transplantation in the rabbit: a model for preservation studies. *Lab Anim* **12**, 63-70 (1978).

50. C. J. E. Watson, P. J. Friend, L. P. Marson, in *Kidney Transplantation - Principles and Practice (Eighth Edition),* S. J. Knechtle, L. P. Marson, P. J. Morris, Eds. (Elsevier, Philadelphia, 2019), pp. 157-172.

Author contributions:

Conceptualization: RYZ, PS, WJZ, YX, ZZ, BZT

Methodology: RYZ, PS, TJW, HY, WH, JD, XDW, SWZ

Investigation: RYZ, PS,

Visualization: RYZ, YCW, LPZ, ZJQ

Supervision: YX, WJZ, ZZ, BZT

Writing—original draft: RYZ, YX, ZJQ

Writing—review & editing: YX, ZZ, BZT